



# Finite element modeling of multiple water droplets impact onto a rough surface: Re-assessing $S_a$ and surface wavelength

J. Xie<sup>a,\*</sup>, P. Chen<sup>a</sup>, D. Rittel<sup>b</sup>

<sup>a</sup> State Key Laboratory of Explosion Science and Technology, Beijing Institute of Technology, 100081, Beijing, PR China

<sup>b</sup> Faculty of Mechanical Engineering, Technion - Israel Institute of Technology, 32000, Haifa, Israel

## ARTICLE INFO

### Keywords:

Waterjet peening  
Rough surface parameters  
Effective surface area  
Implants

## ABSTRACT

Waterjet peening is a promising green technology for roughening the metallic surface of orthopedic and dental implants in order to promote osseointegration. The current conventional surface characterization is essentially based on the arithmetic mean height ( $S_a$ ), without additional considerations, in particular the effective surface area. Yet, this parameter together with the surface energy, is determinant for the cell-implant interaction. The influence of waterjet peening on the surface topography is investigated numerically by generating 9 rough surfaces with different initial  $S_a$  and wavelength  $\lambda$ . Among the selected topography descriptors, the maximum pit depth  $S_v$  might be more viable for characterizing the evolution of the rough surface compared to the other 3 roughness parameters,  $S_a$ , maximum peak height  $S_p$  and maximum height  $S_z$ . The Power Spectrum Density of peened surfaces increases overall, compared to the untreated surfaces irrespective of initial  $S_{a0}$  and  $\lambda_0$ . An analytical formula was derived by simplifying a representative single valley as a half ellipsoid, emphasizing the more influential role of the wavelength  $\lambda$  compared to  $S_a$  in determining the effective surface area for cell adhesion.

## 1. Introduction

The characterization of orthopedics implants' surface is of prime importance for their successful integration in the biological environment. Considering dental implants for example, the latter get anchored with time into the jaw-bone by a process referred to as osseointegration (Shemtov-Yona and Rittel, 2015), for which one of the key parameters is the implant surface roughness,  $S_a$  (Wennerberg and Albrektsson, 2009). While this parameter is routinely mentioned in the dental/biomaterial literature, little mention is made of other surface characterization parameters (to be discussed below), and a "golden standard" has been established in which the "optimal" implant surface roughness should be around 1–2  $\mu\text{m}$  (Albrektsson and Wennerberg, 2004). While the exact biophysical mechanism(s) operating during the osseointegration process is still under debate/characterization (Shah et al., 2019, 2014), the implant surface amounts up to its  $S_a$  value without much additional consideration of the surface topography itself (Nagasawa et al., 2016).

Surface morphology plays major role in mediating cell adhesion (Bagherifard et al., 2015; Bigerelle and Anselme, 2005). The investigation results of shot peened 316L stainless samples indicate a significant maintenance of osteoblast adhesion and proliferation as well as a

remarkable decrease in the bacterial adhesion without using any antibiotics compared to non-treated samples (Bagherifard et al., 2015). By multiple analysis of variance, Bigerelle and Anselme demonstrate that neither material composition nor surface roughness amplitude do influence cell proliferation, whereas the surface morphology affects cell proliferation significantly (Bigerelle and Anselme, 2005).

There are several ways to produce a well-designed/controlled surface morphology. While researchers are keen to optimize surface performance using chemical or physical ways, it may be possible to design surface structures that perform the same or even better without introducing foreign (e.g. grit) substances or destroying the original interface (Shemtov-Yona and Rittel, 2016, 2014). In that sense, the waterjet peening (WP) (Arola and McCain, 2000; Barriuso et al., 2011; Lieblich et al., 2016; Taylor, 1995) without any abrasives is both an economic and green technique. Experimental information on this process can be found in (Hashish, 1984), while a series of recent publications presented various numerical procedures to control both the waterjet process (Chillman et al., 2009; Kunaporn et al., 2004; Xie and Rittel, 2017a) and its outcome (Xie et al., 2019; Xie and Rittel, 2018, 2017b).

Among the relevant surface roughness descriptors, it was found that the following are the most visualized height parameters within the sampling area A (Xie et al., 2019): (1)  $S_a$ : the arithmetic mean height;

\* Corresponding author.

E-mail address: [jxie@bit.edu.cn](mailto:jxie@bit.edu.cn) (J. Xie).

**List of symbols**

$ACF_{1D}$	One dimensional autocorrelation function ( $\mu\text{m}^{-1}$ )
$C_{q_x}$	One dimensional power spectrum density ( $\mu\text{m}^3$ )
$L$	Length ( $\mu\text{m}$ )
$Ral$	One dimensional autocorrelation length ( $\mu\text{m}$ )
$Sa$	The arithmetic mean height ( $\mu\text{m}$ )
$Sa_0$	Initial arithmetic mean height ( $\mu\text{m}$ )
$Sal$	Two dimensional autocorrelation length ( $\mu\text{m}$ )
$S_{eff}$	Effective surface area ( $\mu\text{m}^2$ )
$Sp$	The maximum peak height ( $\mu\text{m}$ )
$Sv$	The maximum pit depth ( $\mu\text{m}$ )
$Sz$	The maximum height ( $\mu\text{m}$ ), $Sz = Sp +  Sv $
$Sdq$	Root mean square gradient
$Sdr$	Developed interfacial area ratio

$a, b$ and $c$	Semi-axes of the general ellipsoid in Cartesian coordinate
$f_s$	Sampling frequency
$\tilde{h}_{q_x}$	The Fourier transform of the profile $h_x$ with a length $L$ ( $\mu\text{m}^2$ )
$h_x$	A discrete surface height profile ( $\mu\text{m}$ )
$k$	The spatial separation
$m$	The mean value of the profile ( $\mu\text{m}$ )
$p$	A constant of Knud Thomsen approximation
$q$	The spatial frequency, $q = 1/\lambda$ ( $\mu\text{m}^{-1}$ )
$\Delta x$	The step size ( $\mu\text{m}$ )
$\lambda$	Wavelength ( $\mu\text{m}$ )
$\lambda_0$	Initial wavelength ( $\mu\text{m}$ )
$\sigma^2$	The variance of the profile ( $\mu\text{m}^2$ )

(2)  $Sp$ : the maximum peak height; (3)  $Sv$ : the maximum pit depth; (4)  $Sz$ : the maximum height. Since  $Sv$  is often expressed as a negative number, the maximum height  $Sz = Sp + |Sv|$ .

With that, since  $Sa$  is almost universally and singly used in the clinical literature, it appears that this parameter should be re-examined in the specific context of waterjet peening. One may ask the following question: “Are all  $Sa$ ’s born equal?” In other words, is  $Sa$  sufficient to define unequivocally the surface state so that the outcome of any surface roughening process can be characterized by a single parameter? In order to illustrate that point, one can start with the obvious observation from Fig. 1 that different surfaces with identical  $Sa$  are not identical, would it only be for the characteristic wavelength ( $\lambda$ ) of the surface profile for an ideal periodic surface. This observation becomes more complex for a realistic surface that is no longer periodic but may exhibit some randomness. Height parameters of a rough surface are not sufficient, as they refer only to one particular spatial size of features. Spatial functions, such as the autocorrelation function and the power spectrum density (PSD), offer a means to further analyze the characteristics of the surface (B Jacobs et al., 2016).

Another important, yet seldom considered parameter, is that of the effective surface area and its evolution following any processing treatment, keeping in mind that the physical properties of the surface (e.g. surface energy (Anderson, 2005)), are always specific, thereby normalized by the effective area. It has been speculated that providing more surface area available for contact with bone can increase the success in obtaining and maintaining optimal osseointegration (Quaranta et al., 2016). Bhushan (1998) summarized the research development of the multiple asperity contact for two rough surfaces in tribology and inspired by his review we developed a simple analytical model to predict the surface area available for contact with bone.

The present paper considers random surfaces of 3 different  $Sa$ ’s, while for each  $Sa$  a subgroup of 3 different  $\lambda$ ’s is generated. All surfaces are subjected to the same waterjet peening, which the process is

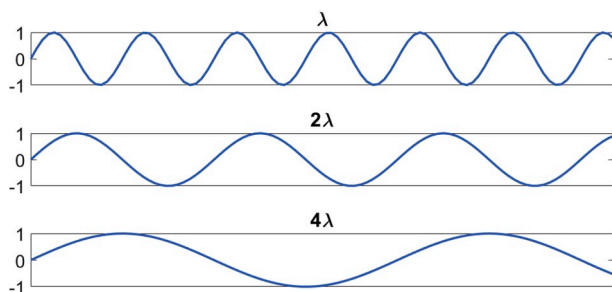


Fig. 1. Schematic illustration of different surface profiles with different wavelength  $\lambda$ . Note the difference in profiles despite the same  $Sa$ .

modeled using the finite element method. The outcome of this numerical study is the evolution of the surface roughness parameters as well as the estimation of the effective surface area of the processed target using the above-mentioned spectral analysis.

While the influence of surface roughness on cell aggregation and growth has been investigated in many works as discussed above, the selection of parameters that would adequately describe the surface morphology is still a subject for discussion. Moreover, the controllability of this morphology and its evolution are seldom evoked at the benefit of an initial  $Ra$  value. Regardless of the selected surface roughening process, it is desirable to have a predictive capability of the surface morphology, in this case using (but not restricted to) waterjet peening. It is believed that such information is an essential starting point for future biological/clinical studies on cell adhesion to roughened surfaces.

Consequently, the paper discusses the evolution of the surface morphology under waterjet peening, and the key parameters that describe it best. In addition, we briefly touch upon a notion that has not been extensively explored, namely the effective surface area of the implant, as “seen” by the cells. Here, we propose a highly simplified model that, while not reflecting the complex reality of a rough surface, provides nevertheless some qualitative insights into the subject.

Consequently, the paper is organized as follows. Section 2 gives the computational model information which includes rough surface generation, surface characterization methods and finite element model. Simulation results of height parameters, autocorrelation length, PSD and the effective surface area are presented and analyzed in section 3 followed by a discussion of the results in section 4. Throughout this work, the objective is to gain insight into the effect of  $Sa$  and  $\lambda$  of the rough surface on the effective surface area that available for cell adhesion.

## 2. The computational model

### 2.1. Rough surface generation

Rough surface generation method is based on the finite element modeling technique. As schematically illustrated in Fig. 2, different rough surfaces were generated by modifying the height (Y-axis in Fig. 2) of several (arbitrarily set to 5) mesh layers elements. First, create a solid part as usual and discretize it into a uniform mesh structure. Second, produce some random heights with different wavelengths. Third, assign the new heights to the corresponding nodes and form an artificial rough surface. Fig. 3 displays some examples of the generated rough surfaces by using this method.

In this work, a total of 9 rough surfaces (Table 1) were generated with 3 different initial  $Sa$  ( $Sa_0$ ) values and 3 different initial  $\lambda$  ( $\lambda_0$ ) values ( $3 \times 3$ ). The 3 selected  $Sa_0$  values are commonly mentioned in the commercial dental implants’ context. Because the wavelength is seldom

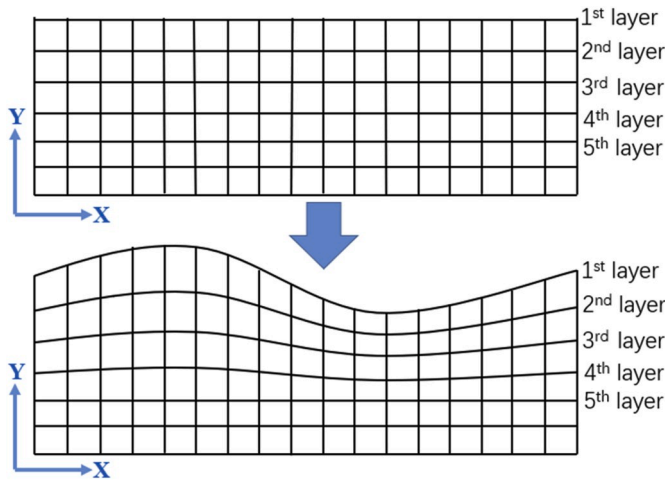


Fig. 2. Generate rough surface by modifying the nodes' heights.

reported in the literature and product brochure, we choose 2/4/8 times to mesh size for the qualitative demonstration of the effect of wavelength. The mesh size is roughly 4.7  $\mu\text{m}$  in the finite element model (as developed hereafter), thus the selected wavelength is 9.4/18.8/37.6  $\mu\text{m}$ , respectively.

## 2.2. Surface characterization

Four areal roughness parameters,  $Sa$ ,  $Sp$ ,  $Sv$  and  $Sz$ , are utilized to characterize the surface topography evolution. Each parameter is normalized by using its increment with respect to its initial value (i.e.,  $(Sx_n - Sx_0)/Sx_0 = \Delta Sx/Sx_0$ ,  $x \in \{a, p, v, z\}$ ,  $n$  being an integer).

### 2.2.1. Autocorrelation length

Because the generated rough surface is not a regular periodic surface, using a single wavelength value to characterize the spatial roughness is inaccurate. A specific roughness parameter, named  $Sal$  (the Autocorrelation Length), is used to quantitatively measure the distance along the surface by which one would find a texture that is statistically different from the original location, so that  $Sal$  can be simply considered as a dominant wavelength of a rough surface.

$Sal$  is the horizontal distance in the direction in which the autocorrelation function (ACF) decays the fastest (Blateyron, 2013). In the present work, the generated rough surface is in-plane isotropic so that 1D ACF (denoted as  $ACF_{1D}$ ) is used to simplify the calculation. The mathematical definition of the  $ACF_{1D}$  for a profile  $h_x$  with a length  $L$  is given in (Zhang and Sundararajan, 2005):

$$ACF_{1D} = \frac{1}{L\sigma^2} \sum_{x=1}^{L-k} (h_x - m)(h_{x+k} - m) \quad (1)$$

where  $k$  is the spatial separation, and  $m$  and  $\sigma^2$  are the mean value and variance of the profile, respectively. We denote discrete functions using subscripts  $h_x$  throughout this manuscript.

Thus, the 1D autocorrelation length  $Ral$  is the length at which the  $ACF_{1D}$  drops between the upper and lower confidence bounds. If the corresponding spatial separation is  $k$ , then

$$Ral_k = \Delta x \cdot k \quad (2)$$

where the  $\Delta x$  is the step size, i.e. the mesh size in the present work.

### 2.2.2. Power spectral density

PSD provides a representation of the amplitude of a surface's roughness as a function of the spatial frequency  $q$ , ( $q = 1/\lambda$ ), of the roughness. Several excellent references rigorously describe the calculation of the PSD, such as (B Jacobs et al., 2016; Elson and Bennett, 1995; Persson et al., 2005). Here too, the 2D PSD is reduced to 1D PSD because of the in-plane isotropy of the generated rough surface, and the 1D PSD denoted as  $C_{q_x}$  is defined as:

$$C_{q_x} = \frac{|\tilde{h}_{q_x}|^2}{L} \quad (3)$$

where  $\tilde{h}_{q_x}$  is the Fourier transform of the profile  $h_x$  with a length  $L$ .  $C_{q_x}$  has units of  $\mu\text{m}^3$  in the present work.

### 2.2.3. Surface area

Despite its relevance to the cell adhesion process, determining the effective surface area of a randomly rough surface is not straightforward, although one may experimentally measure it using the micro-Computed Tomography ( $\mu\text{CT}$ ) analysis (Quaranta et al., 2016). However, an analytical approximation is required here, and for demonstration, a common sinusoidal surface (Fig. 4) is selected as the study object.

The surface area for contact with bone is the whole surface area of the sinusoidal surface as displayed in Fig. 4. Here, for the sake of demonstration only one cycle of the sinusoidal surface is considered (Fig. 5(a)). One cycle of the sinusoidal surface has 2 peaks plus 2 valleys

Table 1

Rough surfaces generated in the present study.

Case Num.	$Sa_0$ ( $\mu\text{m}$ )	$\lambda_0$ ( $\mu\text{m}$ )
Case 1	0.5	9.4
Case 2		18.8
Case 3		37.6
Case 4	1.0	9.4
Case 5		18.8
Case 6		37.6
Case 7	1.5	9.4
Case 8		18.8
Case 9		37.6

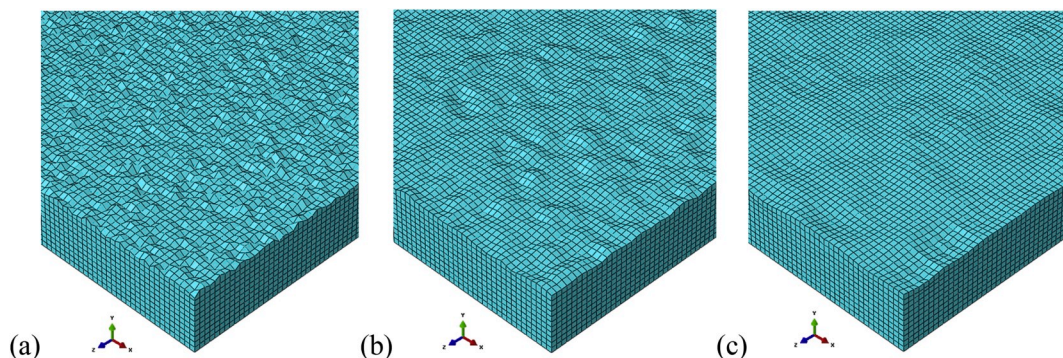


Fig. 3. Partial view of the rough surface of the substrate. (a)  $\lambda$ ; (b)  $2\lambda$ ; (c)  $4\lambda$ .

in total. The peak and valley part have the same surface area due to the symmetry of the sinusoidal surface. So, the total surface area is equivalent to 4 times of the valley (as same as the peak) surface area. The valley (Fig. 5(b)) is further simplified as a half ellipsoid, thus the problem transforms into the determination of the surface area of a half-ellipsoid, denoted as the effective surface area ( $S_{eff}$ ). Note that only one cycle of the sinusoidal surface is chosen, therefore the equation derived later is only valid for observing the trend rather than obtaining an accurate value.

The half surface area ( $S_{eff}$ ) for an arbitrary ellipsoid ( $\frac{x^2}{a^2} + \frac{y^2}{b^2} + \frac{z^2}{c^2} = 1$ ) is simplified by using the Knud Thomsen approximation (Xu et al., 2009) as:

$$S_{eff} = 2\pi \left[ \frac{a^p b^p + a^p c^p + b^p c^p}{3} \right]^{\frac{1}{p}} \quad (4)$$

where  $p$  is a constant. This approximation has the least relative error ( $\pm 1.061\%$  in the worst case) when  $p \sim 1.6075$ .

As shown in Fig. 5,  $a$  and  $b$  are equal and their value is one-quarter of the wavelength ( $\lambda/4$ ), while  $c$ , in this case is equal to the absolute value of maximum depth  $Sv$  ( $|-1| = 1$ ). Given the popularity of  $Sa$ , it is preferable to use  $Sa$  instead of  $Sv$  to represent  $c$ . According to its definition,

$$\begin{aligned} Sa &= \frac{1}{A} \iint_A |z(x, y)| dx dy \\ &= \frac{1}{2\pi \cdot 2\pi} \int_0^{2\pi} \int_0^{2\pi} |\cos x \cos y| dx dy \\ &= \frac{4 \cdot 4}{4\pi^2} \int_0^{\frac{\pi}{2}} \int_0^{\frac{\pi}{2}} \cos x \cos y dx dy \\ &= \frac{4}{\pi^2} \end{aligned} \quad (5)$$

and the proportional relation is obtained:

$$\frac{Sv}{Sa} = \frac{c}{Sa} = \frac{1}{\frac{4}{\pi^2}}$$

Then  $c$  is expressed as:

$$c = Sa \cdot \frac{\pi^2}{4} \quad (6)$$

Eq. (4) can now be rewritten by substituting  $a$ ,  $b$  and  $c$  with  $\lambda$  and  $Sa$ , to yield the expression for the surface area of a half ellipsoid  $S_{eff}$

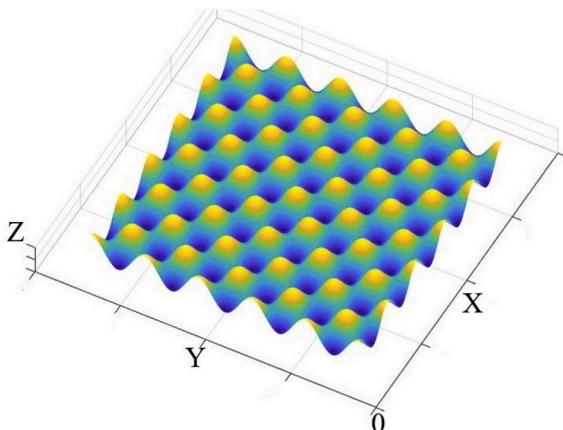


Fig. 4. A schematic diagram of a sinusoidal surface.

$$S_{eff} = 2\pi \left[ \frac{\left(\frac{\lambda}{4}\right)^{2p} + 2\left(\frac{\lambda}{4}\right)^p \left(Sa \frac{\pi^2}{4}\right)^p}{3} \right]^{\frac{1}{p}} = \frac{\pi}{8} \lambda \left[ \frac{\lambda^p + 2\pi^{2p} Sa^p}{3} \right]^{\frac{1}{p}} \quad (7)$$

### 2.3. Finite element model

The model for the analysis of the jet generation and impingement as well as the solid part of the model (the target) was reported in detail in Ref.(Xie et al., 2019). For the sake of brevity, we will only mention here a few key details.

A representative model (Fig. 6(a)) that contains 100 droplets with different diameters is created for simulating the waterjet impingement. A total of 10 rounds (of 100 droplets each) are run for a typical simulation. Each batch of 100 droplets is divided into 10 groups (distinguished by using different colors in Fig. 6(a)), where every group has the same droplet diameter which ranges from 10  $\mu\text{m}$  to 100  $\mu\text{m}$ . The choice of 10 classes of diameters has been explained by Xie and Rittel (2017b), basically because of the high inlet pressure of waterjet peening, and the atomization effect of waterjet. Taking Arola's experiment (Arola et al., 2001) as an example, for 280 MPa inlet pressure case, the maximum velocity at standoff distance 150 mm is 711 m/s, so 700 m/s is chosen as the impact velocity in the present study.

The 3D Coupled Eulerian Lagrangian (CEL) model was constructed using the commercial software Abaqus/Explicit (Dassault Systèmes Simulia Corporation, 2014). The dimensions of the target (Lagrangian domain) and droplets domain (Eulerian domain) are set as indicated in Fig. 6(b) and (c), respectively. Since the length (equals to the width) is 600 $\mu\text{m}$ , and the mesh seeds are 128 ( $2^7$ ), the mesh size is 600/128  $\approx$  4.7 $\mu\text{m}$ . Note this value is used before in Table 1 for determining  $\lambda_0$ , and in Eq. (2) as the step size. The EC3D8R element (an 8-node linear Eulerian brick with reduced integration) and C3D8R element (an 8-node linear hexahedral element with reduced integration) are used for the Eulerian and Lagrangian domain, respectively. The substrate bottom surface is constrained against all displacements and rotations.

Ti6Al4V was selected as the substrate (target) material for its being one of the most favored implant materials in dentistry due to its satisfactory biocompatibility, excellent corrosion resistance and a relative low specific weight (Moon et al., 2017). The Johnson-Cook plasticity model (Johnson and Cook, 1983) and the Mie-Grüneisen equation of state are used to describe the deformation behaviors of Ti6Al4V and water droplets, and their properties used in the simulation are shown in Table 2 (Dorogoy and Rittel, 2009; Hamashima, 2004).

## 3. Results

### 3.1. Height parameters

We will now present the evolution of various roughness parameters ( $Sa$ ,  $Sp$ ,  $Sv$ ,  $Sz$ ) according to Table 1. Note that each parameter is normalized by using its increment with respect to its initial value ( $(Sx_n - Sx_0)/Sx_0 = \Delta Sx/Sx_0$ ,  $x \in \{a, p, v, z\}$ ,  $n$  is an integer).

Starting with  $Sa$ , one can note from Fig. 7 that the normalized  $Sa$  change during the 10 rounds impingement depends more on the initial wavelength  $\lambda_0$ . If  $\lambda_0$  is small ( $\lambda_0 = 9.4\mu\text{m}$ ), then the normalized  $Sa$  declines always (blue lines, Fig. 7); on the contrary, if  $\lambda_0$  is larger ( $\lambda_0 = 37.6\mu\text{m}$ ), then the normalized  $Sa$  increases always (yellow lines, Fig. 7); for the medium cases ( $\lambda_0 = 18.8\mu\text{m}$ ), the normalized  $Sa$  barely changes (red lines, Fig. 7). This conclusion holds for the rough surfaces with different initial  $Sa$ .

Considering now the parameter  $Sp$  in Fig. 8, one can see that the evolution of the normalized  $Sp$  has some similarities as well as some differences compared to the change of the normalized  $Sa$ . The same thing is that, regardless of the initial  $Sa$ , the change in the normalized  $Sp$  is affected by the initial wavelength  $\lambda_0$  (Fig. 8). The different thing is that

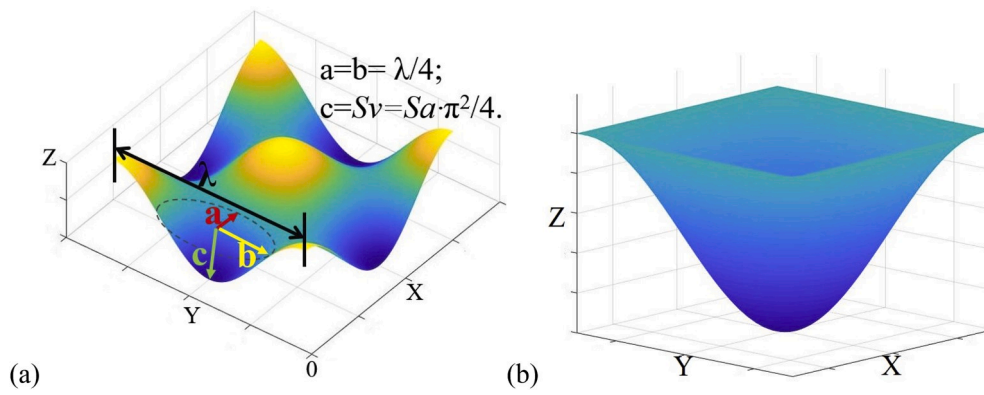


Fig. 5. (a) One cycle ( $2\pi$ ) of a sinusoidal surface; (b) the valley is simplified as a half ellipsoid.

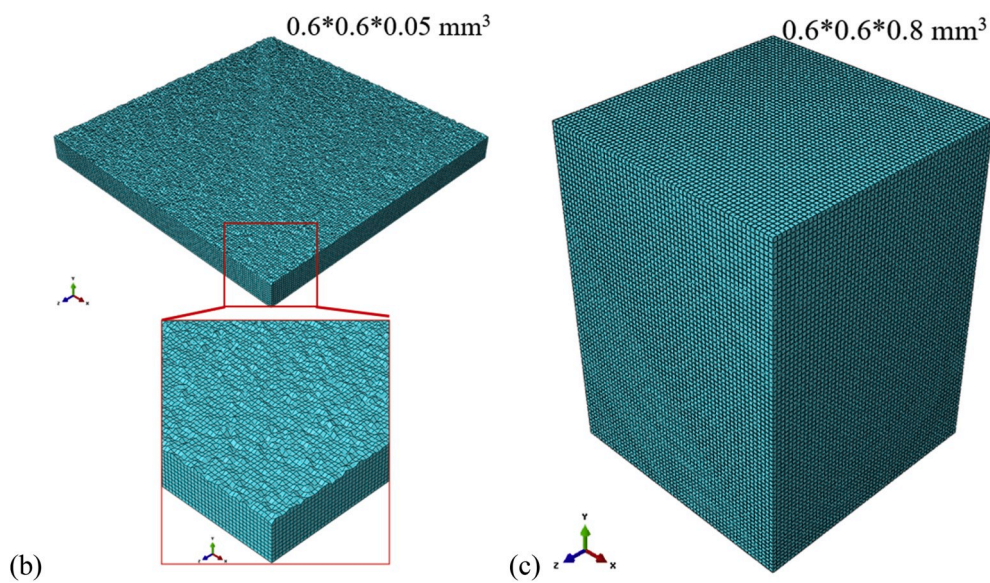
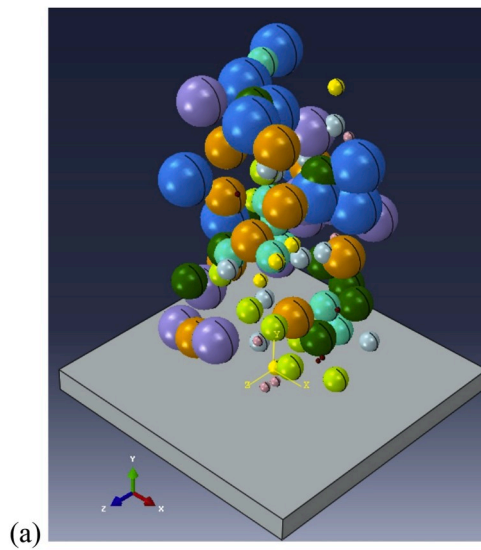


Fig. 6. (a) The multiple droplets model; (b) the mesh structure of Eulerian domain; (c) the mesh structure of Lagrangian domain (case 4).

for  $\lambda_0 = 37.6\mu\text{m}$  cases, the normalized  $Sp$  has little change, whereas the normalized  $Sp$  increases for  $\lambda_0 = 18.8\mu\text{m}$  cases.

Unlike the former two parameters, the normalized  $Sv$  is influenced

both by initial  $Sa$  and  $\lambda_0$  resulting in very complex evolution history (Fig. 9), thus a complex evolutionary history of the normalized  $Sz$  too (Fig. 10).  $Sz$  is a combination of  $Sp$  and  $Sv$ , but obviously the evolution of

**Table 2**  
Material properties used in the simulation.

Properties (Unit)	Ti6Al4V (Dorogoy and Rittel, 2009)	Water (Hamashima, 2004)
Density, $\rho$ (kg/m <sup>3</sup> )	$8.9 \times 10^3$	$1 \times 10^{-3}$
Viscosity, $\nu$ (Pa-s)		$1 \times 10^{-3}$
Sound velocity, $c_0$ (m/s)		1476
Slope of $U_s$ vs $U_p$ , $s$		2
Grüneisen coefficient, $\Gamma_0$		1.65
Young's modulus, $E$ (GPa)	114	
Poisson ratio, $\nu$	0.342	
Yield stress, $A$ (MPa)	880	
Hardening constant, $B$ (MPa)	695	
Hardening exponent, $n$	0.36	
Strain rate constant, $C$	0.04	
Melting temperature, $T_m$ (K)	1660	
Reference temperature, $T_0$ (K)	273	

$Sp$  ( $Sv$ ) is influenced by  $Sa_0$ . Note that for smaller  $Sa_0$ ,  $Sv$  evolves more significantly. A similar trend is observed for  $Sp$  at larger  $Sa_0$ . Consequently, for the roughest surface ( $Sa_0 = 1.5\mu\text{m}$ )  $Sz$  has a tendency similar to that of  $Sp$ , whilst for the surface with  $Sa_0 = 0.5\mu\text{m}$ ,  $Sz$  and  $Sv$  have shown small differences.

3.2. Autocorrelation length

Table 3 presents the 1D autocorrelation length ( $Ral$ ) calculated using Eq. (1) and Eq. (2) for the various cases listed in Table 1. Comparing the  $Ral$  before and after 10 rounds impingement for the 9 investigated rough surfaces, one can see that for a rough surface with a larger  $Sa_0$  and  $\lambda_0$ ,  $Ral$  barely changes after 10 rounds impingement. Looking at case 9 ( $Sa_0 = 1.5\mu\text{m}$ ,  $\lambda_0 = 37.6\mu\text{m}$ ) as an example,  $Ral$  before and after the impingements are roughly the same. However, considering case 1 ( $Sa_0 = 0.5\mu\text{m}$ ,  $\lambda_0 = 9.4\mu\text{m}$ ), one can note that  $Ral$  increases up to 4 times. This may be the result of many new asperities with longer wavelengths being produced by continuous impingements.

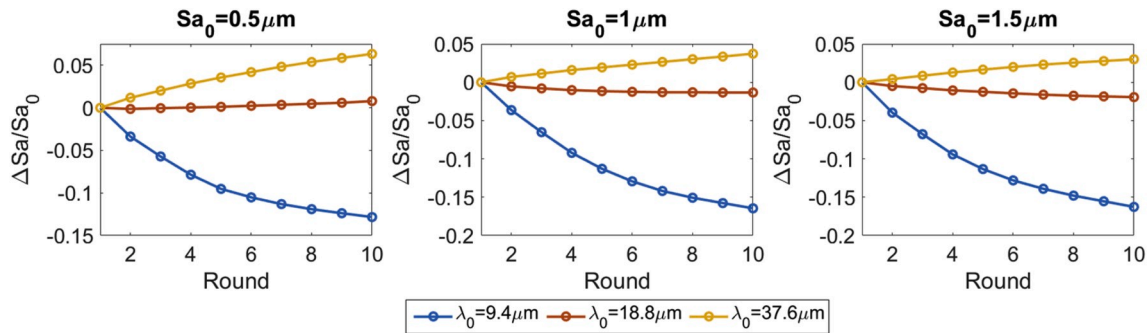


Fig. 7. The evolution of the normalized arithmetic mean height  $Sa$  with different  $Sa_0$  and  $\lambda_0$ .

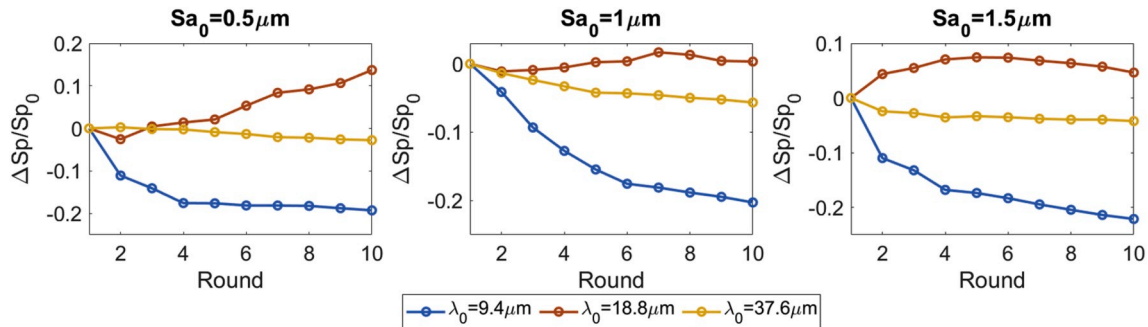


Fig. 8. The evolution of the normalized maximum peak height  $Sp$  with different  $Sa_0$  and  $\lambda_0$ .

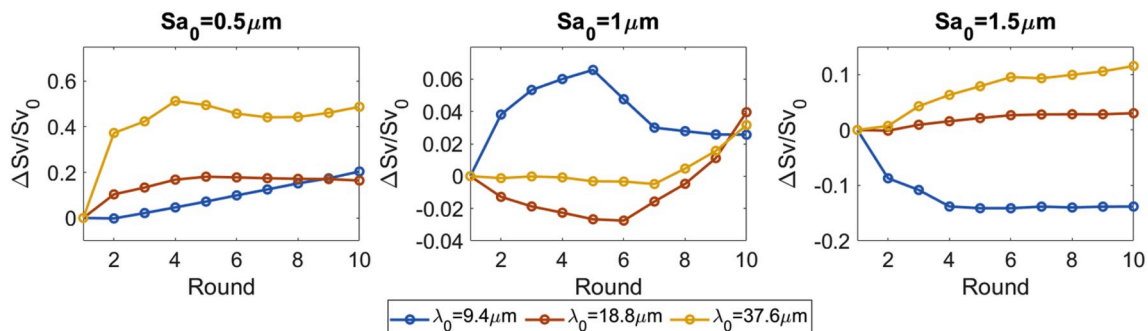


Fig. 9. The evolution of the normalized maximum pit depth  $Sv$  with different  $Sa_0$  and  $\lambda_0$ .

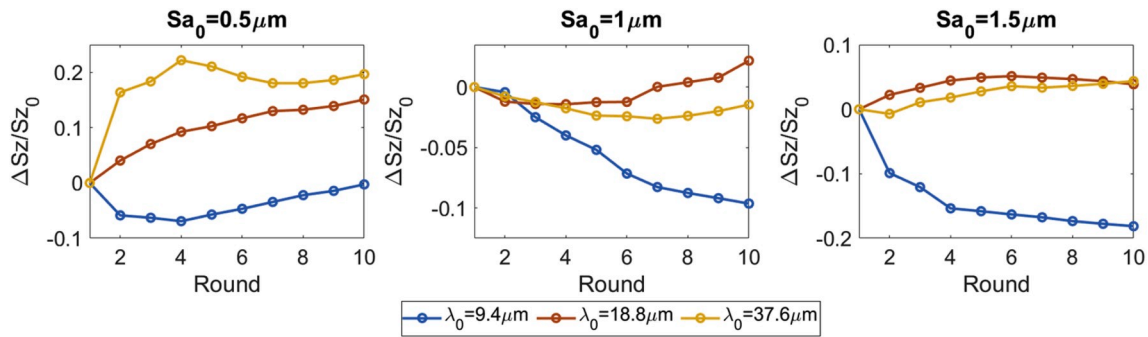


Fig. 10. The evolution of the normalized maximum height  $Sz$  with different  $Sa_0$  and  $\lambda_0$ .

Table 3

The autocorrelation length before and after the impingements.

$Ral$ ( $\mu\text{m}$ )	$Sa_0 = 0.5\mu\text{m}$		$Sa_0 = 1\mu\text{m}$		$Sa_0 = 1.5\mu\text{m}$	
	Before	After	Before	After	Before	After
$\lambda_0 = 9.4\mu\text{m}$	4.7	18.8	4.7	14.1	4.7	14.1
$\lambda_0 = 18.8\mu\text{m}$	14.1	23.5	14.1	18.8	18.8	18.8
$\lambda_0 = 37.6\mu\text{m}$	32.9	37.6	28.2	28.2	28.2	28.2

3.3. PSD

The PSD profiles for the study cases listed in Table 1 are shown in Figs. 11–13. Because the height data of rough surface are extracted element by element and the element size is  $4.7\mu\text{m}$ , the sampling frequency  $f_s$  is 0.21 ( $f_s = \Delta x^{-1} \approx 0.21$ ), which is also the maximum spatial frequency  $q$  for the PSD analysis. According to the Nyquist sampling theorem, the highest frequency of the rough surface therefore should be no more than  $0.21/2$ , i.e. the minimum  $\lambda$  that can be captured is  $2 \times 4.7 = 9.4\mu\text{m}$ .

From Figs. 11–13, one can see that the PSDs of impinged surfaces (denoted as *after*) overall increase compared to the untreated surfaces (denoted as *before*) no matter what  $Sa_0$  and  $\lambda_0$ , but there are still some subtle differences. For the rough surfaces with the largest  $\lambda_0$  ( $37.6\mu\text{m}$ , Fig. 13), the spectra before and after WP impingements are structural (peaks' locations) similar, only the intensities of peaks increase in proportion after the impingements. By contrast, the variations of peaks' positions, as well as the amplitudes in the other two figures (Figs. 10 and 11), are slightly different. On the one hand, the locations of some peaks shift after the impingements; on the other hand, the rise of amplitudes is uneven, some locations increase larger whilst some locations increase smaller. Through the comparison of these 3 figures, it seems that WP has a negligible influence on the  $\lambda$  composition of a surface if this surface already has a longer  $\lambda_0$ , whereas if the  $\lambda_0$  is relatively smaller, then droplets impingements would change the composition of  $\lambda$  of the peened surface.

3.4. Surface area

The estimated effective surface area ( $S_{eff}$ ) (done according to Eq. (7)) is plotted as a function of  $Sa$  and  $\lambda$ , as shown in Fig. 14. Obviously, the surface area has a positive correlation with both  $Sa$  and  $\lambda$ . However, one must verify which of  $Sa$  and  $\lambda$  contributes more to the increase of surface area? The answer lies in Fig. 15.

First, the derivative of  $S$  with respect to  $Sa$  ( $\partial S/\partial Sa$ ) for 3 given  $\lambda$  values is plotted in Fig. 15(a). These lines can be interpreted as the surface area growth rate as a function of  $Sa$  for a fixed  $\lambda$  value.  $\partial S/\partial Sa$  it goes up rapidly at first then flattens out, meaning that the growth rate of surface area would remain steady at length. By contrast, the derivative of  $S$  with respect to  $\lambda$  ( $\partial S/\partial \lambda$ ) for 3 given  $Sa$  values as shown in Fig. 15 (b) exhibits a different trend.  $\partial S/\partial \lambda$  rises slowly initially, then climbs up steeply, so that as long as the  $\lambda$  keeps increasing the surface area would increase faster. This fact reveals that for a given  $\lambda$  a slight change of  $Sa$  will cause a dramatic increase of surface area at the beginning then tends to be gentle; whilst for a given  $Sa$ , monotonically increasing  $\lambda$  does not increase the surface area effectively since the maximum value of  $\partial S/\partial \lambda$  is only around 17 that is lower than the general values of  $\partial S/\partial Sa$ . One may therefore conclude that within the investigated range of values,  $\lambda$  is more influential than  $Sa$  in determining the effective surface area.

4. Discussion

4.1. Roughness parameters

The roughness parameters considered in the present work are first the *height* parameters ( $Sa$ ,  $Sp$ ,  $Sv$ ,  $Sz$ ), and then the *spatial* parameters ( $Ral$ , PSD).

Because the surface is subject to the impact loading, the valley parts ( $Sv$ ) exhibits a more significant change than the other parameters, reflecting differences both in the  $Sa_0$  and  $\lambda_0$  together (Fig. 7).  $Sv$  could thus be a good indicator for characterizing the evolution of the rough surface.

The main advantage of using PSD to characterize the rough surface is

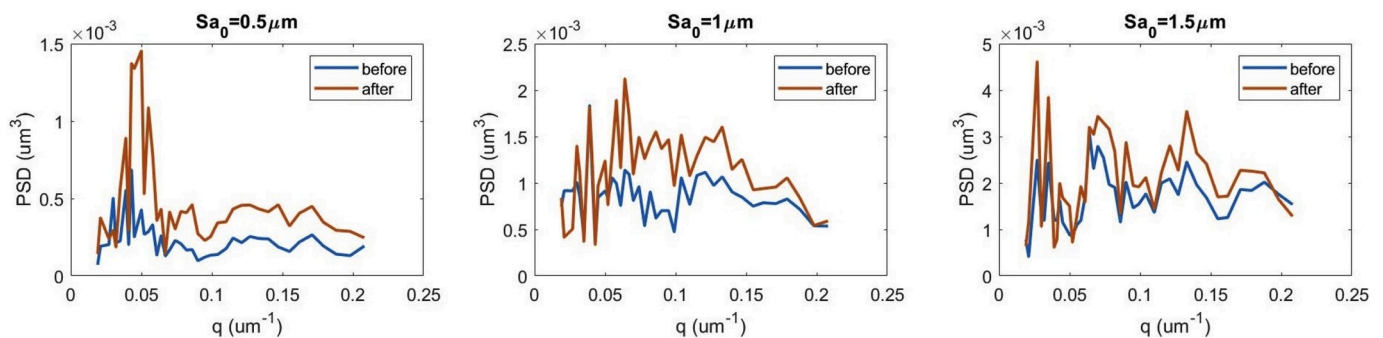


Fig. 11. Power spectrum density of the profiles of the rough surface with  $\lambda_0 = 9.4\mu\text{m}$ .

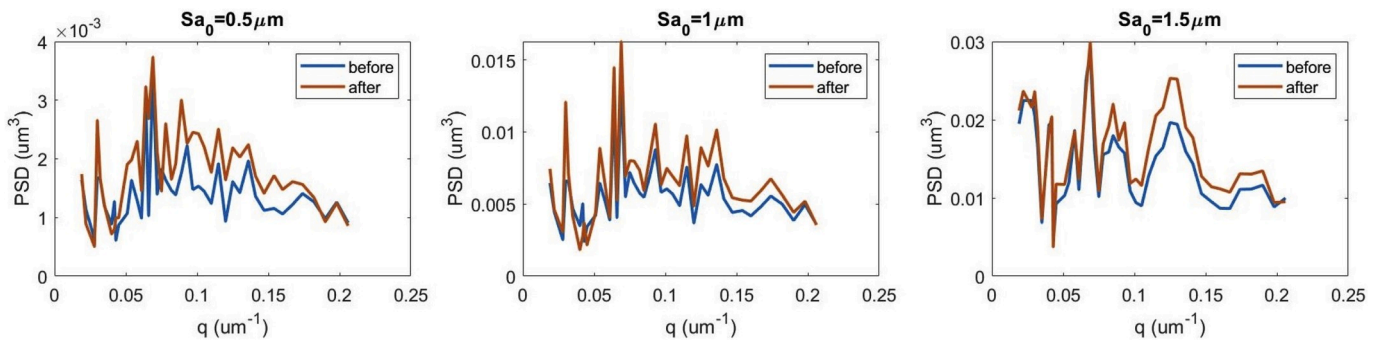


Fig. 12. Power spectrum density of the profiles of the rough surface with  $\lambda_0 = 18.8\mu\text{m}$ .

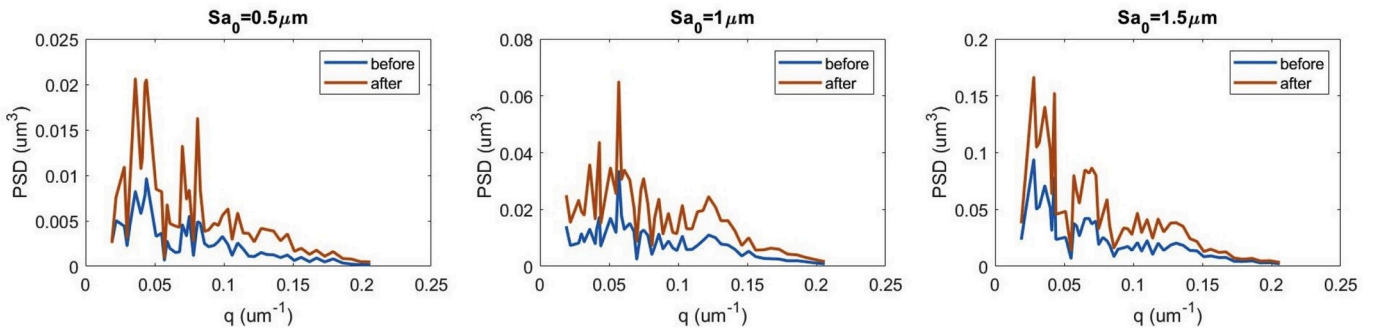


Fig. 13. Power spectrum density of the profiles of the rough surface with  $\lambda_0 = 37.6\mu\text{m}$ .

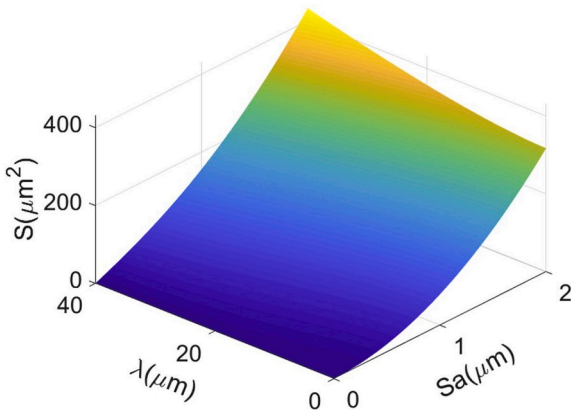


Fig. 14. The estimated surface area as a function of  $S_a$  and  $\lambda$ .

that PSD is qualified through the full spectral range of interest that reflects the speed, feed data, sources of noise and so on of the waterjet. Due to the dimension limits of the model developed in the current work, the investigated frequency's range is quite narrow ( $1/0.6\text{mm}$  to  $1/4.7\mu\text{m}$ , i. e.  $0.002$  to  $0.21 \mu\text{m}^{-1}$ ), the PSD spectra presented in section 3.3 can not express the information of the surfaces whose wavelengths are beyond this range. A larger size model should be created next step, making sure that the PSD analysis can comprise all the interest frequencies relating to the WP process.

#### 4.2. Effective surface area

Beyond the above-mentioned topographic parameters, we also considered the effective surface area and its evolutions, such as to better interpret and quantify the implant surface based on the readily available height and spatial roughness parameters. The effective surface area can be understood as the net implant surface area available for cell adhesion.

In the preliminary model illustrated in Fig. 5(a), one valley is treated

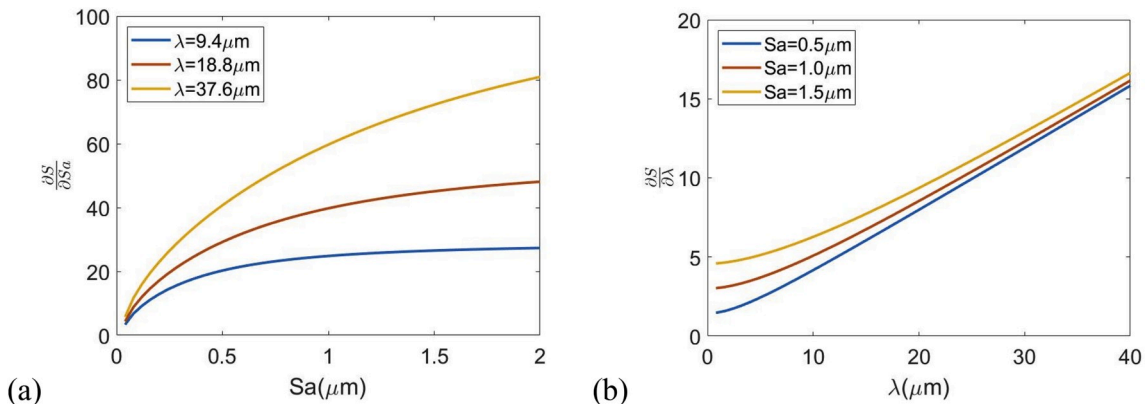


Fig. 15. The derivative of surface area (a) with respect to  $S_a$  at different  $\lambda$  values and (b) with respect to  $\lambda$  at different  $S_a$  values.

as a representative example for calculating the surface area. Within the investigated range,  $\lambda$  is a more critical factor in determining the effective surface area compared to  $S_a$ , as seen by comparing the values reported in Fig. 15(a) and (b). Practically, regarding dental implant for example, the implant surface should be controlled to have a profitable longer  $\lambda$  plus an appropriate higher  $S_a$  ( $S_a$  is not always the higher the better), that is meaning more effective surface area, for boosting cell adhesion.

The above conclusion is drawn based on a single valley, and it does not reflect the general reality. An extension of the present approach would have necessarily to be of a stochastic nature. Eq. (7) relates the effective area to both the wavelength  $\lambda$  and  $S_a$ .  $S_a$  is an average value, so we keep it fixed. However, one can think of a statistical representation of  $\lambda$  provided e.g. by spectral analysis. This would in turn generate a distribution of “local” effective areas, the sum of which would represent the overall area of a roughened surface.

### 4.3. Hybrid parameters

Since the height and spatial parameters are discussed in the present work, a hybrid parameter based on the slope feature of the surface would be useful for characterizing the surface morphology.

The gradient of a surface point is defined for each axis  $x$  and  $y$  by  $\partial z/\partial x$  and  $\partial z/\partial y$ , thus the root mean square gradient ( $Sdq$ ) is then calculated on the whole surface with

$$Sdq = \sqrt{\frac{1}{A} \iint_A \left[ \left( \frac{\partial z(x,y)}{\partial x} \right)^2 + \left( \frac{\partial z(x,y)}{\partial y} \right)^2 \right] dx dy} \quad (8)$$

Taking the sinusoidal surface (Fig. 5) as an example, the  $Sdq$  would be

$$\begin{aligned} Sdq &= \sqrt{\frac{1}{2\pi \cdot 2\pi} \int_0^{2\pi} \int_0^{2\pi} \left[ \left( \frac{\partial \cos x \cos y}{\partial x} \right)^2 + \left( \frac{\partial \cos x \cos y}{\partial y} \right)^2 \right] dx dy} \\ &= \frac{1}{2\pi} \sqrt{\int_0^{2\pi} \int_0^{2\pi} [(-\sin x \cos y)^2 + (-\cos x \sin y)^2] dx dy} \\ &= \frac{1}{2\pi} \sqrt{\int_0^{2\pi} \left( \int_0^{2\pi} \sin^2 x dx \right) \cos^2 y dy + \int_0^{2\pi} \left( \int_0^{2\pi} \cos^2 x dx \right) \sin^2 y dy} \\ &= \frac{1}{2\pi} \sqrt{\int_0^{2\pi} \pi \cos^2 y dy + \int_0^{2\pi} \pi \sin^2 y dy} = \frac{1}{2\pi} \sqrt{\pi \cdot \pi + \pi \cdot \pi} = \frac{\sqrt{2}}{2} \end{aligned} \quad (9)$$

Therefore, for a typical sinusoidal surface, the general slope would be  $\sqrt{2}/2$ . This value can be used to calculate the developed interfacial area ratio  $Sdr$ :

$$Sdr = \frac{\text{rough surface area} - \text{cross sectional area}}{\text{cross sectional area}} \quad (10)$$

Using a simple plane for demonstration (Fig. 16) if the slope increases from 0 to  $\sqrt{2}/2$ , the developed interfacial area ratio would be around 0.225. This parameter is used as a measure of the surface area growth, because a perfectly flat and smooth surface would have  $Sdr = 0$ . To quantitatively investigate the effective surface area, these two hybrid parameters  $Sdq$  and  $Sdr$  are recommended to be considered.

## 5. Conclusions

- $S_v$  seems to be a better indicator in order to characterize the evolution of the rough surface compared to the other 3 roughness parameters.
- The PSDs of impinged surfaces increase overall compared to the untreated surfaces, irrespective of  $S_{a0}$  and  $\lambda_0$ .

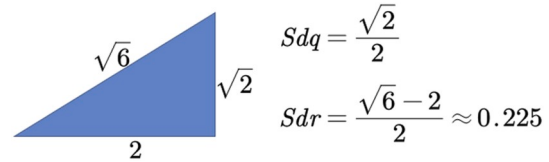


Fig. 16. The developed interfacial area ratio.

- An expression for the effective surface area  $S_{eff}$  was developed, based on  $S_a$  and  $\lambda$ , by using a representative single valley model, and an analytical formula was derived by simplifying the valley as a half ellipsoid.
- Within the investigated range of values,  $\lambda$  is more influential than  $S_a$  in determining the effective surface area.
- Introducing the probability distribution of the valley to the model, and the hybrid roughness parameters should be considered to quantitatively investigate the effective area growth.

## Declaration of competing interest

The authors declare that there is no potential conflict of interest.

## Acknowledgments

The work is supported at the Beijing Institute of Technology by Research Fund Program for Young Scholars.

## References

Albrektsson, T., Wennerberg, A., 2004. Oral implant surfaces: Part 1—review focusing on topographic and chemical properties of different surfaces and in vivo responses to them. *Int. J. Prosthodont.* (IJP) 17, 536–543. <https://doi.org/10.1098/rsta.2009.0062>.

Anderson, T.L., 2005. *Fracture Mechanics: Fundamentals and Applications*, third ed. CRC Press, Boca Raton. CRC Press.

Arola, D., McCain, L., 2000. Abrasive waterjet peening: a new method of surface preparation for metal orthopedic implants. *J. Biomed. Mater. Res.* 53, 536–546.

Arola, D., McCain, M.L., Kunaporn, S., Ramulu, M., 2001. Waterjet and abrasive waterjet surface treatment of titanium: a comparison of surface texture and residual stress. *Wear* 249, 943–950. [https://doi.org/10.1016/S0043-1648\(01\)00826-2](https://doi.org/10.1016/S0043-1648(01)00826-2).

B Jacobs, T.D., Junge, T., Pastewka, L., 2016. Quantitative characterization of surface topography using spectral analysis. *Surf. Topogr. Metrol. Prop.* <https://doi.org/10.1088/2051-672X/0/0/000000>, 0, 000000.

Bagherifard, S., Hickey, D.J., de Luca, A.C., Malheiro, V.N., Markaki, A.E., Guagliano, M., Webster, T.J., 2015. The influence of nanostructured features on bacterial adhesion and bone cell functions on severely shot peened 316L stainless steel. *Biomaterials* 73, 185–197. <https://doi.org/10.1016/j.biomaterials.2015.09.019>.

Barriuso, S., Lieblich, M., Multigner, M., Etxebarria, I., Alberdi, A., González-Carrasco, J. L., 2011. Roughening of metallic biomaterials by abrasiveless waterjet peening: characterization and viability. *Wear* 270, 634–639. <https://doi.org/10.1016/j.wear.2011.01.024>.

Bhushan, B., 1998. Contact mechanics of rough surfaces in tribology: multiple asperity contact. *Tribol. Lett.* 4, 1–35.

Bigerelle, M., Anselme, K., 2005. Statistical correlation between cell adhesion and proliferation on biocompatible metallic materials. *J. Biomed. Mater. Res.* 72A, 36–46. <https://doi.org/10.1002/jbm.a.30212>.

Blateyron, F., 2013. The areal field parameters. In: *Characterisation of Areal Surface Texture*. Springer Berlin Heidelberg, Berlin, Heidelberg, pp. 15–43. [https://doi.org/10.1007/978-3-642-36458-7\\_2](https://doi.org/10.1007/978-3-642-36458-7_2).

Chillman, A., Ramulu, M., Hashish, M., 2009. A general overview of waterjet surface treatment modeling. In: *American WJTA Conference and Expo*.

Dassault Systèmes Simulia Corporation, 2014. Aabqus V. 6.14 documentation. Abaqus 6.14. <https://doi.org/10.1017/CBO9781107415324.004>.

Dorogoy, A., Rittel, D., 2009. Determination of the johnson-cook material parameters using the SCS specimen. *Exp. Mech.* 49, 881–885. <https://doi.org/10.1007/s11340-008-9201-x>.

Elson, J.M., Bennett, J.M., 1995. Calculation of the power spectral density from surface profile data. *Appl. Optic.* 34, 201. <https://doi.org/10.1364/AO.34.000201>.

Hamashima, H., 2004. Determination of JWL parameters for non-ideal explosive. *AIP Conf. Proc.* 706, 331–334. <https://doi.org/10.1063/1.1780246>.

Hashish, M., 1984. A modeling study of metal cutting with abrasive waterjets. *J. Eng. Mater. Technol.* 106, 88. <https://doi.org/10.1115/1.3225682>.

Johnson, G.R., Cook, W.H., 1983. A constitutive model and data for metals subjected to large strains, high strain rates and high temperatures. 7th Int. Symp. Ballist. <https://doi.org/10.1038/nrm3209>.

- Kunaporn, S., Ramulu, M., Jenkins, M.G., Hashish, M., 2004. Residual stress induced by waterjet peening: a finite element analysis. *J. Pressure Vessel Technol.* 126, 333. <https://doi.org/10.1115/1.1767175>.
- Lieblich, M., Barriuso, S., Ibanez, J., Ruiz-de-Lara, L., Diaz, M., Ocana, J.L., Alberdi, A., Gonzalez-Carrasco, J.L., 2016. On the fatigue behavior of medical Ti6Al4V roughened by grit blasting and abrasiveless waterjet peening. *J. Mech. Behav. Biomed. Mater.* 63, 390–398. <https://doi.org/10.1016/j.jmbbm.2016.07.011>.
- Moon, B.S., Kim, S., Kim, H.E., Jang, T.S., 2017. Hierarchical micro-nano structured Ti6Al4V surface topography via two-step etching process for enhanced hydrophilicity and osteoblastic responses. *Mater. Sci. Eng. C* 73, 90–98. <https://doi.org/10.1016/j.msec.2016.12.064>.
- Nagasawa, M., Cooper, L.F., Ogino, Y., Mendonca, D., Liang, R., Yang, S., Mendonca, G., Uoshima, K., 2016. Topography influences adherent cell regulation of osteoclastogenesis. *J. Dent. Res.* 95, 319–326. <https://doi.org/10.1177/0022034515616760>.
- Persson, B.N.J., Albohr, O., Tartaglino, U., Volokitin, A.I., Tosatti, E., 2005. On the nature of surface roughness with application to contact mechanics, sealing, rubber friction and adhesion. *J. Phys. Condens. Matter* 17. <https://doi.org/10.1088/0953-8984/17/1/R01>.
- Quaranta, A., D'Isidoro, O., Bambini, F., Putignano, A., 2016. Potential bone to implant contact area of short versus standard implants. *Implant Dent.* 25, 97–102. <https://doi.org/10.1097/ID.0000000000000357>.
- Shah, F., Nilson, B., Brånemark, R., Thomsen, P., Palmquist, A., 2014. The bone-implant interface - nanoscale analysis of clinically retrieved dental implants. *Nanomed. Nanotechnol. Biol. Med.* 10, 1729–1737. <https://doi.org/10.1016/j.nano.2014.05.015>.
- Shah, F., Thomsen, P., Palmquist, A., 2019. Osseointegration and current interpretations of the bone-implant interface. *Acta Biomater.* 84, 1–15. <https://doi.org/10.1016/j.actbio.2018.11.018>.
- Shemtov-Yona, K., Rittel, D., 2016. Fatigue of dental implants: facts and fallacies. *Dent. J.* 4, 1–11. <https://doi.org/10.3390/dj4020016>.
- Shemtov-Yona, K., Rittel, D., 2015. An overview of the mechanical integrity of dental implants. *BioMed Res. Int.* <https://doi.org/10.1155/2015/547384>.
- Shemtov-Yona, K., Rittel, D., 2014. Identification of failure mechanisms in retrieved fractured dental implants. *Eng. Fail. Anal.* 38, 58–65. <https://doi.org/10.1016/j.engfailana.2014.01.002>.
- Taylor, T.A., 1995. Surface roughening of metallic substrates by high pressure pure waterjet. *Surf. Coating. Technol.* 76–77, 95–100. [https://doi.org/10.1016/0257-8972\(95\)02528-6](https://doi.org/10.1016/0257-8972(95)02528-6).
- Wennerberg, A., Albrektsson, T., 2009. On implant surfaces: a review of current knowledge and opinions. *Int. J. Oral Maxillofac. Implants* 25, 63–74. <https://doi.org/10.1111/j.1600-051X.2008.01321.x>.
- Xie, J., Rittel, D., 2018. The effects of waterjet peening on a random-topography metallic implant surface. *Eur. J. Mech. Solid.* 71, 235–244. <https://doi.org/10.1016/J.EUROMECHSOL.2018.03.022>.
- Xie, J., Rittel, D., 2017a. A two-dimensional model for metallic surface roughness resulting from pure waterjet peening. *Int. J. Eng. Sci.* 120, 189–198. <https://doi.org/10.1016/j.ijengsci.2017.08.010>.
- Xie, J., Rittel, D., 2017b. Three-dimensional stochastic modeling of metallic surface roughness resulting from pure waterjet peening. *Int. J. Eng. Sci.* 120, 241–253. <https://doi.org/10.1016/j.ijengsci.2017.08.011>.
- Xie, J., Rittel, D., Chen, P., 2019. Modeling the topographic evolution of a rough metallic surface resulting from impact of water droplets. *Int. J. Eng. Sci.* 144, 103142. <https://doi.org/10.1016/j.ijengsci.2019.103142>.
- Xu, D., Cui, J., Bansal, R., Hao, X., Liu, J., Chen, W., Peterson, B.S., 2009. The ellipsoidal area ratio: an alternative anisotropy index for diffusion tensor imaging. *Magn. Reson. Imaging* 27, 311–323. <https://doi.org/10.1016/j.mri.2008.07.018>.
- Zhang, Y., Sundararajan, S., 2005. The effect of autocorrelation length on the real area of contact and friction behavior of rough surfaces. *J. Appl. Phys.* 97, 103526. <https://doi.org/10.1063/1.1914947>.